Mathematical Modeling for 2D Light--Sheet Fluorescence Microscopy image reconstruction

Article *in* Inverse Problems · March 2020

DOI: 10.1088/1361-6420/ab80d8

6 authors, including:

Evelyn Cueva
University of Chile
3 PUBLICATIONS **3** CITATIONS
SEE PROFILE

Axel Osses
University of Chile
54 PUBLICATIONS **726** CITATIONS
SEE PROFILE

Victor Castañeda
University of Chile
27 PUBLICATIONS **144** CITATIONS
SEE PROFILE

Benjamin Palacios
University of Chicago
7 PUBLICATIONS **27** CITATIONS
SEE PROFILE

Mathematical Modeling for 2D Light–Sheet Fluorescence Microscopy image reconstruction

Evelyn Cueva[1], **Matias Courdurier**[2], **Axel Osses**[1], **Victor Castañeda**[3], **Benjamin Palacios**[4], **Steffen Härtel**[3].

[1] Departamento de Ingeniería Matemática and Centro de Modelamiento Matemático, UMI CNRS 2807, FCFM, Universidad de Chile, Chile

[2] Facultad de Matemáticas, Pontificia Universidad Católica de Chile, Chile

[3] Laboratory for Scientific Image Analysis SCIANLab, Facultad de Medicina, Universidad de Chile, Chile

[4]Department of Statistics, University of Chicago, US

E-mail: `ecueva@dim.uchile.cl`

Abstract. We study an inverse problem for Light Sheet Fluorescence Microscopy (LSFM), where the density of fluorescent molecules needs to be reconstructed. Our first step is to present a mathematical model to describe the measurements obtained by an optic camera during an LSFM experiment. Two meaningful stages are considered: excitation and fluorescence. We propose a paraxial model to describe the excitation process which is directly related with the Fermi pencil–beam equation. For the fluorescence stage, we use the transport equation to describe the transport of photons towards the detection camera. For the mathematical inverse problem that we obtain after the modeling, we present a uniqueness result, recasting the problem as the recovery of the initial condition for the heat equation in $\mathbb{R} \times (0, \infty)$ from measurements in a space–time curve. Additionally, we present numerical experiments to recover the density of the fluorescent molecules by discretizing the proposed model and facing this problem as the solution of a large and sparse linear system. Some iterative and regularized methods are used to achieve this objective. The results show that solving the inverse problem achieves better reconstructions than the direct acquisition method that is currently used.

Keywords: LSFM, Fermi pencil–beam equation, radiative transport equation, backward uniqueness, heat equation.

1. Introduction

Modern microscopy techniques allow researchers to observe phenomena on a sub–cellular, cellular and supra–cellular level. The observation of cells at different scales gives insights of key biological questions within modern science fostering more and more systematic approaches to understand the essence of life [1]. Contemporary microscopy offers wide spectra of different techniques with distinct advantages and disadvantages. Particularly, fluorescence microscopy allows biologists to observe live specimens and dynamic processes within a tissue or specimen. This technique is based on the addition of fluorescent molecules named fluorophores, which attach to target proteins or cellular structures on a sub–cellular or cellular level like DNA, membranes, cytoskeleton, or extra cellular matrix [23]. Fluorophores are excited by photons, usually a laser beam, and fluorescent emission is captured by a photonic detector or camera. Fluorescence microscopes vary in the excitation procedure, observation and volumetric resolution. In the last decades, fluorescence microscopy became the standard tool for in vivo and in toto (whole sample) imaging, however, photo–toxicity, photo–bleaching, out–of–focus contribution and acquisition speed limit its application.

Particularly, Light Sheet Fluorescence Microscopy (LSFM) is a technique which uses a thin light sheet (plane) to excite the fluorophores in the focal plane of the detection objective [29]. This technique has some advantages compared to the regular confocal fluorescence microscopes. Thanks to the perpendicular excitation through the thin plane, an optical sectioning occurs. This excitation reduces the out–of–focus contribution, due to the light sheet only excites fluorophores present in the observed focal plane. The photo–toxicity and photo–bleaching are also trimmed down (the energy load is reduced from 10^3 E to E [22, 32]), allowing acquisition of specimen in–vivo for long periods of time. Moreover, the reduced out–of–focus contribution improves the edges and contrast of the images. Additionally, its acquisition speed can achieve a few seconds for an entire 3D scan and it can observe big specimens (in the size of millimeters/centimeters) [35]. Thus, LSFM is currently one of the preferred techniques to acquire a wide range of applications, especially for big specimen and long observation times, obtaining a reasonable image contrast for cell segmentation and time resolution for cell tracking [16]. Another related LSFM technique is the so–called lattice light–sheet microscopy where the laser beam consists in a very narrow Bessel type lattice, intended to capture much smaller spatial scales of nanometers [10, 31]. In this study, we will only consider LSFM with gaussian type laser beams.

During the image acquisition process, it occurs that the farther we are from the point of light emission, the higher the loss of image resolution (see e.g. Figure 2 in [20] and Figure 3 in [21]). We also see an increasing dominance of blur and shadows as the laser goes through the object [20, 30]. The standard reconstruction procedure used to overcome these issues consists of merging different images by using the opposite and complementary excitation directions [21, 20, 30] (left and right), as in the three images in Figure 1. This process is feasible in practice since the design of the microscope structure is set up in such a way that the laser beam can illuminate the object from opposite sides preventing the interference of the lasers. A critical problem with this merging process is the presence of artifacts in the middle plane of the final images. On the other hand, there exist calibration problems in the experimental setting for the acquisition process, such as: errors in the position and orientation of the lasers respect to the cameras, object displacements, opposite laser correspondence, etc.

To avoid this merging technique and hence improve the final images, we establish a mathematical model that allows us to understand the laser behaviour and the subsequent fluorescence process. Even more, we propose to study this imaging technique as an inverse problem, where we seek to reconstruct the distribution μ of the fluorophore from the set of (images) measurements obtained by the camera.

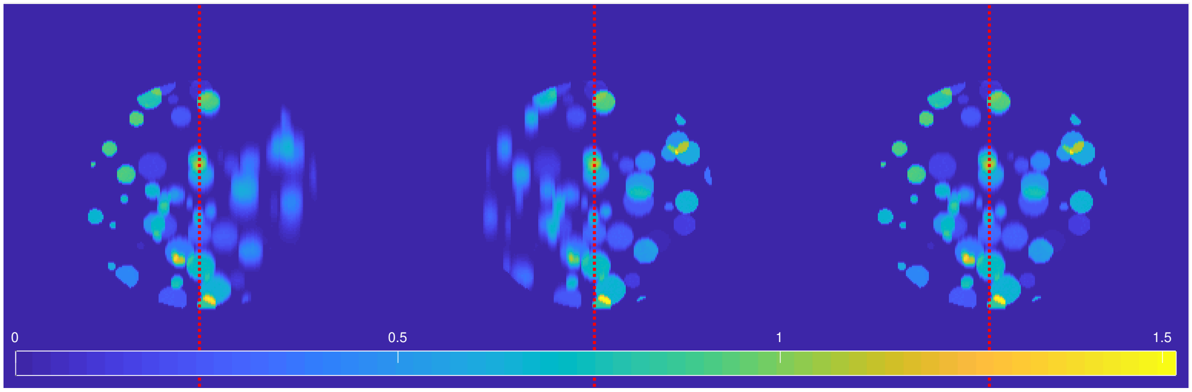

Figure 1: An example of a LSFM image (density of the fluorescent molecules μ). The first and second images show the scattering effects observed by the camera when left and right excitations are applied. The third one is the "fused image", taking the best side of the previous ones (as in [20, 21]).

In Section 2, we first describe an operator $\mathcal{P}$ that relates the measurements with our unknown variable μ, identifying two meaningful stages in an LSFM experiment: excitation and fluorescence. To model the first stage, we use the Fermi–Eyges pencil–beam equation to describe the space and angular distributions of the laser beam when it propagates in a near–transparent object. This equation was first presented by Fermi in 1940 and studied later by Rossi and Greisen in [33, Section 23]. In [7, 8], Börgers *et al.* present an asymptotic derivation of the Fermi Pencil–Beam equation from the Fokker–Planck equation and from the linear Boltzmann equation under two different conditions.

On the other hand, the fluorescence stage takes place once the fluorescent molecules has been activated by the laser beam. For the second stage we use the Radiative Transport Equation (RTE) (see e.g. [2]) to describe how the photons propagate until reaching the collimated camera. In this way, we completely define the forward operator $\mathcal{P}$ describing the proposed mathematical model.

In Section 3 we summarize the mathematical model obtained and the description of the inverse problem that we will study.

In Section 4 we show that there is unique reconstruction of the function μ in the proposed inverse problem. Injectivity of the operator $\mathcal{P}$ is presented in Theorem 1. We obtain this results by considering the relationship between the solutions of the Fermi pencil–beam and heat equations. By interpreting our measurements in terms of heat propagation, we obtain injectivity of $\mathcal{P}$ by reducing the problem to one of backward uniqueness for a heat equation from a nontrivial space–time curve, and the uniqueness for such problem is presented in Section 5.

Finally, in Sections 6 and 7, we present a discretization version of the forward operator to numerically solve the direct and inverse problems. We propose to find a numerical solution for the LSFM reconstruction problem by solving a linear system. In this context, we use different algorithms that are already available to optimally solve this problems. Mainly, we refer to [17, 18, 13] where discrete inverse problems are studied and iterative regulatization methods for sparse and large–scale problems are detailed.

2. Mathematical model in LSFM

2.1. Notation and model scheme

Let $\Omega \subset \mathbb{R}^2$ be an open set with smooth boundary, which represents the object studied under the microscope. We assume that Ω is contained in the rectangle $[0, s_1] \times [-y_1, y_1]$, for some $s_1 > 0$, $y_1 > 0$, both large enough. And for each $h \in [-y_1, y_1]$ we define $x_h := \inf\{x : (x, h) \in \Omega\}$ (see in Figure 2 the corresponding terms).

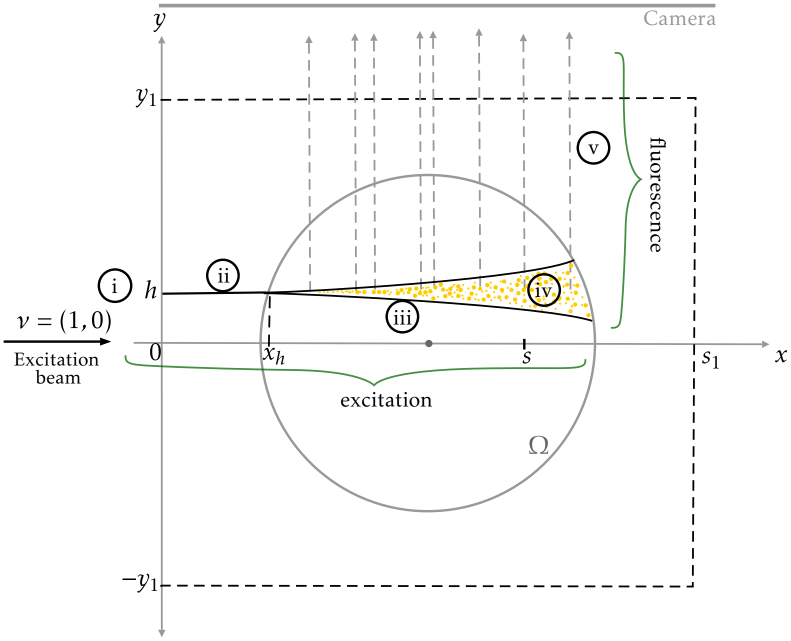

Figure 2: Geometric representation of the excitation and emission beams. An incident laser at point $(0, h)$ illuminates the object from left and propagates inside the object according to the Fermi pencil–beam equation, exciting the fluorescent molecules within the sample. Then, the excited fluorescence molecules emits photons in all directions. For collimated cameras, only photons emitted in straight vertical directions are detected at different positions s.

The modelling of the LSFM experiment has two main stages, excitation and fluorescence, that are divided in the following components (see Figure 2):

(i) The excitation beam is emitted at the point $(0, h)$ in the direction $\nu = (1, 0)$. We call $h \in [-y_1, y_1]$ the *height of incidence*.

(ii) The laser follows a free transport equation, without attenuation or scattering, until entering the domain Ω at the point (x_h, h).

(iii) Once the laser enters the object, the propagation of the laser is described by the Fermi pencil–beam equation (equation (3)). We denote by $u := u_h(x, y, \boldsymbol{\omega})$ the intensity of photons at position $(x, y) \in [0, s_1] \times [-y_1, y_1]$ traveling in the direction $\boldsymbol{\omega} = (\cos(\omega), \sin(\omega))$ for $\omega \in \mathbb{R}/2\pi\mathbb{Z}$. Therefore, the total intensity of excitation photons at (x, y), arising from an incident excitation at $(0, h)$, is $v_h(x, y) = \int u_h(x, y, \boldsymbol{\omega}) d\boldsymbol{\omega}$.

(iv) The excitation beam reaching (x, y) excites the fluorescent molecules at that point, and the excited fluorophores will be proportional to the density of fluorescent molecules and the excitation intensity. Namely, if $\mu(x, y)$ is the density of fluorescent molecules at (x, y), then the excited fluorophores will be $w_h(x, y) = c\, v_h(x, y)\mu(x, y)$, where c is the activation constant.

(v) The excited fluorescence molecules w_h emit photons in all directions, which propagates according to a linear transport equation (equation (8)). The camera is vertically collimated, hence only measuring those photons traveling in the direction $(0, 1)$. We will denote by $p_h(s)$ the fluorescent measurement at pixel $s \in [0, s_1]$ arising from an excitation at $(0, h)$.

The previous description of LSFM considers some simplifications and does not include all the possible physical phenomena involved in LSFM. The proposed model is a step in trying to understand and tackle difficulties observed in LSFM, like blurring effects among others, and an attempt in trying to improve such imaging technique by analyzing the simplified and related inverse problem. LSFM can be considered as a particular illumination-detection geometrical setting of Fluorescence Molecular Tomography (FMT) (a review of Fluorescence Molecular Imaging and Fluorescence Molecular Tomography can be found in [28] and [38]), but for a less diffusive media as the one usually considered in FMT. This less diffusive media implies a number of differences between our approach and the usual descriptions used in FMT, namely, in FMT the photon propagation is usually described by a diffusion equation without directionality of photons (see e.g. equation (1) in [24], and equations (1) and (2) in [38]), which translates into a very different mathematical equation for the illumination model. Furthermore, the detection model generally employed in FTM does not allow for directional collimation, and also requires measurements from multiple angles (see e.g. [28] and [38]).

In the next subsection we present more details about stages (iii) and (v) that we have briefly introduce above.

2.2. Excitation: the Fermi pencil–beam equation

In this part we look into the details of stage (iii) above, *i.e.* the propagation of the excitation laser inside the object described by the Fermi pencil–beam equation.

To describe the transport of photons in highly scattering and highly peaked forward regime, a possible model is the following Fokker–Planck equation (see [2]),

$$\boldsymbol{\omega} \cdot \nabla u(\boldsymbol{x}, \boldsymbol{\omega}) + \lambda(\boldsymbol{x}, \boldsymbol{\omega}) u(\boldsymbol{x}, \boldsymbol{\omega}) = \psi(\boldsymbol{x}) \Delta_{\boldsymbol{\omega}} u(\boldsymbol{x}, \boldsymbol{\omega}) \tag{1}$$

where, $\boldsymbol{x} = (x, y) \in \mathbb{R}^2$ and $\boldsymbol{\omega} \in S^1$ is the direction of propagation, with $\boldsymbol{\omega} = (\cos(\omega), \sin(\omega))$ for $\omega \in \mathbb{R}/2\pi\mathbb{Z}$. The quantity $u(\boldsymbol{x}, \boldsymbol{\omega})$ corresponds to the intensity of photons at the point $\boldsymbol{x}$ that are moving in the direction $\boldsymbol{\omega}$. The coefficient $\lambda := \lambda_h(\boldsymbol{x}, \boldsymbol{\omega})$ represents the portion of photons that have been absorbed at the point $\boldsymbol{x}$ that were moving in direction $\boldsymbol{\omega}$. The operator $\Delta_{\boldsymbol{\omega}}$ is the Laplace–Beltrami operator on S^1 and $\psi(\boldsymbol{x})$ is the diffusion coefficient related to the scattering of the medium. In isotropic media (when $\lambda(\boldsymbol{x},\boldsymbol{\omega})=\lambda(\boldsymbol{x})$) and since we are in $\mathbb{R}^2$ (letting $\boldsymbol{\omega}=(\cos(\omega),\sin(\omega))$), we can rewrite the Fokker–Planck equation (1) as

$$Lu(\boldsymbol{x},\omega)=(\cos(\omega)\partial_x+\sin(\omega)\partial_y+\lambda(\boldsymbol{x})-\psi(\boldsymbol{x})\partial_\omega^2)u(\boldsymbol{x},\omega)=0. \tag{2}$$

And in the case that the diffusion coefficient $\psi(\boldsymbol{x})$ is small enough and the source is spatially and directionally concentrated, the photons will concentrated along a line and direction determined by the source. Namely, in [8] it was shown that under adequate smallness and ellipticity assumptions on the diffusion coefficient, the Fokker–Plank equation

$$\begin{aligned}&Lu(x,y,\omega)=\big(\cos(\omega)\partial_x+\sin(\omega)\partial_y+\lambda(\boldsymbol{x})-\psi(\boldsymbol{x})\partial_\omega^2\big)\,u(x,y,\omega)=0.\\&u(x_h,y,\omega)=\delta_h(y)\delta_0(\omega),\qquad x\in(x_h,\infty),y\in\mathbb{R},\omega\in\mathbb{R}/2\pi\mathbb{Z},\end{aligned}$$

admits a *paraxial approximation* with $\omega\sim 0$, given by the Fermi pencil–beam equation

$$\begin{aligned}&L_{\text{approx}}u(x,y,\omega)=\big(\partial_x+\omega\partial_y+\lambda(x,h)-\psi(x,h)\partial_\omega^2\big)\,u(x,y,\omega)=0.\\&u(x_h,y,\omega)=\delta_h(y)\delta_0(\omega),\qquad x\in(x_h,\infty),y\in\mathbb{R},\omega\in\mathbb{R},\end{aligned} \tag{3}$$

here we have considered the approximations below inasmuch as ω is concentrated around zero and satisfies:

$$\cos(\omega)\approx 1,\quad \sin(\omega)\approx\omega$$

and

$$|\omega|\ll 1,\ \omega\in\mathbb{R}/2\pi\mathbb{Z}\iff|\omega|\ll 1,\ \omega\in\mathbb{R}.$$

The Fermi equation has been derived from Fokker–Planck in [7] by means of stereographic–type coordinates on the unit circle and by dropping higher order terms coming from asymptotic expansions with respect to the diffusion magnitude.

Let $\lambda_h(x)=\lambda(x,h)$ and $\psi_h(x)=\psi(x,h)$. Equation (3) can be explicitly solved (see e.g. [12]) and the solution for $x\in(x_h,\infty),\ y\in\mathbb{R},\ \omega\in\mathbb{R}$ is given by

$$u_h(x,y,\omega)=\exp\left(-\int_{x_h}^{x}\lambda_h(\tau)d\tau\right)f_Z(\boldsymbol{z}), \tag{4}$$

where $\boldsymbol{z} = ((y-h) - \omega(x - x_h), \omega)^\top$, and where

$$f_Z(\boldsymbol{z}) = \frac{1}{2\pi\sqrt{\det \Sigma(x,h)}} \cdot \exp\left[-\frac{1}{2}\boldsymbol{z}^\top \Sigma^{-1}(x,h)\boldsymbol{z}\right],$$

with

$$\Sigma(x,h) := \begin{pmatrix} E_2 & -E_1 \\ -E_1 & E_0 \end{pmatrix}(x,h), \qquad \Sigma^{-1}(x,h) = \frac{1}{\det \Sigma}\begin{pmatrix} E_0 & E_1 \\ E_1 & E_2 \end{pmatrix}(x,h),$$

and

$$E_k(x,h) = \int_{x_h}^{x} (\tau - x_h)^k \psi_h(\tau) d\tau, \quad k = 0,1,2. \tag{5}$$

By letting $\Lambda = \begin{pmatrix} 1 & (x - x_h) \\ 0 & 1 \end{pmatrix}$ (hence $\det(\Lambda) = 1$ and $\Lambda^{-1} = \begin{pmatrix} 1 & -(x - x_h) \\ 0 & 1 \end{pmatrix}$) then

$$\boldsymbol{z} = \begin{pmatrix} (y-h) - \omega(x - x_h) \\ \omega \end{pmatrix} = \Lambda^{-1}\begin{pmatrix} y - h \\ \omega \end{pmatrix},$$

and

$$f_Z(\boldsymbol{z}) = \frac{1}{2\pi\sqrt{\det \Lambda\Sigma(x,h)\Lambda^\top}} \cdot \exp\left[-\frac{1}{2}\begin{pmatrix} y-h \\ \omega \end{pmatrix}^\top \left(\left(\Lambda^{-1}\right)^\top \Sigma^{-1}(x,h)\Lambda^{-1}\right)\begin{pmatrix} y-h \\ \omega \end{pmatrix}\right].$$

Denoting $\alpha^2 = (\Lambda\Sigma\Lambda^\top)_{11} = (E_2(x,h) - 2(x - x_h)E_1(x,h) + (x - x_h)^2 E_0(x,h))$ we get (the marginal distribution on a multivariate normal distribution),

$$\int_{\mathbb{R}} f_Z(\boldsymbol{z}) dw = \frac{1}{\alpha\sqrt{2\pi}} \exp\left(-\frac{(y-h)^2}{2\alpha^2}\right).$$

From the solution (4), the previous calculation gives us the total excitation intensity at a point $(x,y) \in (x_h, \infty) \times (-y_1, y_1)$ arising from an incident excitation at $(0,h)$, namely

$$\begin{aligned} v_h(x,y) &= \int_{\mathbb{R}} u_h(x,y,w) dw = \exp\left(-\int_{x_h}^{x} \lambda_h(\tau) d\tau\right) \int_{\mathbb{R}} f_Z(\boldsymbol{z}) dw \\ &= \frac{1}{\alpha_h(x)\sqrt{2\pi}} \exp\left(-\int_{x_h}^{x} \lambda_h(\tau) d\tau\right) \exp\left(-\frac{(y-h)^2}{2\alpha_h^2(x)}\right), \end{aligned} \tag{6}$$

where

$$\begin{aligned}\alpha_h^2(x) &= \big(E_2(x,h) - 2(x-x_h)E_1(x,h) + (x-x_h)^2E_0(x,h)\big)\\ &= \int_{x_h}^{x} \psi_h(\tau)[(\tau-x_h)^2 - 2(x-x_h)(\tau-x_h) + (x-x_h)^2]d\tau\\ &= \int_{x_h}^{x} (x-\tau)^2\psi_h(\tau)d\tau. \qquad (7)\end{aligned}$$

We can notice that for a fix x, $v_x(y) = v_h(x,y)$ in (6) is the density function of a univariate normal distribution with mean h and variance $\alpha_h^2(x)$ multiplied by an exponential term depending on λ_h. This is explained in detail in Figure 3.

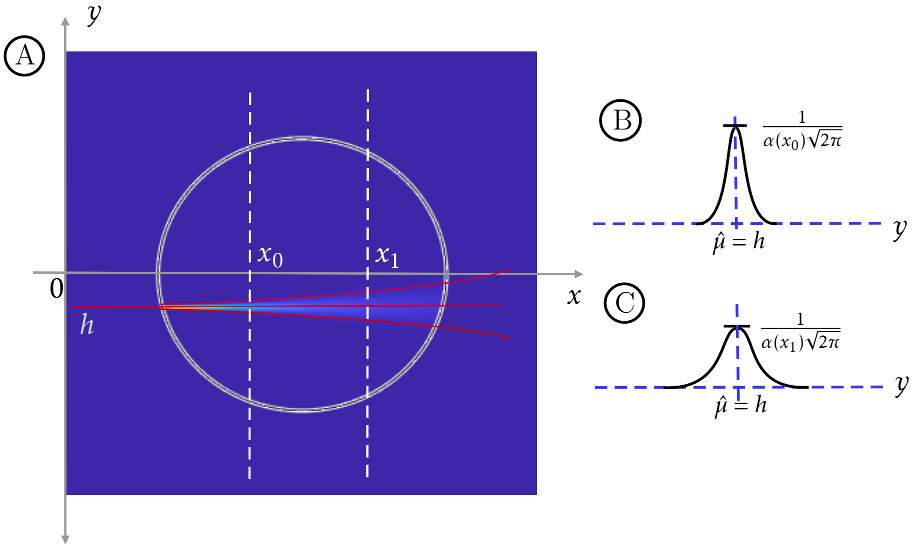

Figure 3: Graphic interpretation of equation (6). Figure A shows the function v_h when an illumination is made at height $y = h$. For fix points x_0 and x_1, the expressions $v_h(x_0, \cdot)$ and $v_h(x_1, \cdot)$ are the density distribution of a normal distribution multiplied by a constant that depends on λ_h. Figures B and C show these normal distributions. In both cases, the mean is $\hat{\mu} = h$ with variance $\alpha^2(x_0)$ and $\alpha^2(x_1)$, respectively.

Given the excitation intensity $v_h(x,y)$ and density of fluorescent molecules $\mu(x,y)$, the fluorescent source is $w_h(x,y) = c\, v_h(x,y)\mu(x,y)$, and in the following we provide the details of the model that relates the sources of photons and the measurements obtained at the camera, using the linear transport equation.

2.3. Fluorescence: Radiative Transfer Equation

In this detection stage we assume a perfect collimation of the camera in the direction $(0,1)$, this means that only photons travelling parallel to the y–axis are measured.

The collimation at the camera allows us to remove the positive contribution in the measurements of the scattered photons.

Let us denote by $p_h(\boldsymbol{x}, \boldsymbol{\theta})$ the intensity of photons at position $\boldsymbol{x} \in \mathbb{R}^2$ traveling in a direction $\boldsymbol{\theta} \in S^1$, arising from an incident excitation at $(0, h)$. We will consider that the propagation of photons is governed by a linear transport equation with attenuation a and source w_h (see [4, 5]), namely we will assume that p_h satisfies,

$$\begin{aligned} \boldsymbol{\theta} \cdot \nabla_{\boldsymbol{x}}\, p_h(\boldsymbol{x}, \boldsymbol{\theta}) + a(\boldsymbol{x}) p_h(\boldsymbol{x}, \boldsymbol{\theta}\,) = w_h(\boldsymbol{x}), \quad \forall \boldsymbol{x} \in \mathbb{R}^2,\ \boldsymbol{\theta} \in S^1 \\ \lim_{t \to \infty} p_h(\boldsymbol{x} - t\boldsymbol{\theta}, \boldsymbol{\theta}\,) = 0, \quad \forall \boldsymbol{x} \in \mathbb{R}^2,\ \boldsymbol{\theta} \in S^1, \end{aligned} \tag{8}$$

where the boundary condition states that there are no external radiation sources, and w_h is supported inside Ω. Under mild regularity conditions on w_h and a, the unique solution of equation (8) is

$$p_h(\boldsymbol{x}, \boldsymbol{\theta}) = \int_{-\infty}^{0} w_h(\boldsymbol{x} + r\boldsymbol{\theta}) \exp\left(- \int_{r}^{0} a(\boldsymbol{x} + \tau\boldsymbol{\theta}) d\tau \right) dr,$$

hence providing an expression for the intensity of photons detected at position $\boldsymbol{x}$ if collimated in direction $\boldsymbol{\theta}$.

Since the cameras are outside the bounded object supporting the source, it is useful to consider the total number of photons traveling along lines. In order to do so, let us parametrize the lines in the plane as $L(s, \boldsymbol{\theta}^{\perp}) = \{\boldsymbol{x} \in \mathbb{R}^2 \colon \boldsymbol{x} \cdot \boldsymbol{\theta} = s\}$, where $s \in \mathbb{R}$ is the distance of the line to the origin, $\boldsymbol{\theta} \in S^1$ is the direction perpendicular to the line, and $\boldsymbol{\theta}^{\perp}$, the rotation of $\boldsymbol{\theta}$ by $\pi/2$, is the direction of the line. The total intensity of photons along the line $L(s, \boldsymbol{\theta}^{\perp})$ is

$$\begin{aligned} p_h(s, \boldsymbol{\theta}^{\perp}) &= \lim_{\tau \to \infty} p_h(\tau\boldsymbol{\theta}^{\perp} + s\boldsymbol{\theta}, \boldsymbol{\theta}^{\perp}) \\ &= \int_{\mathbb{R}} w_h(r\boldsymbol{\theta}^{\perp} + s\boldsymbol{\theta}) \exp\left(- \int_{r}^{\infty} a(\tau\boldsymbol{\theta}^{\perp} + s\boldsymbol{\theta}) d\tau \right) dr \\ &= c \int_{\mathbb{R}} \mu(r\boldsymbol{\theta}^{\perp} + s\boldsymbol{\theta}) v_h(r\boldsymbol{\theta}^{\perp} + s\boldsymbol{\theta}) \exp\left(- \int_{r}^{\infty} a(\tau\boldsymbol{\theta}^{\perp} + s\boldsymbol{\theta}) d\tau \right) dr, \end{aligned} \tag{9}$$

the last equality is obtained by the assumption $w_h(x, y) = c\, v_h(x, y)\mu(x, y)$ described in (iv). The Figure 5 shows an example of the integral along one line.

Under the standard setup of the microscope, the object does not rotate with respect to the camera, hence for the measurements we will consider only the fixed direction $\boldsymbol{\theta}^{\perp} = (0, 1)$. Rewriting (9), and including the expression for v_h given by (6), we can finally write an expression for $p_h(s) = p_h(s,(0,1))$ the intensity of fluorescent photos measured in the camera pixel at position $s \in [0, s_1]$ arising from an incident excitation at height h (see Figure 2):

$$\begin{aligned} p_h(s) &= c \int_{\mathbb{R}} \mu(s,r) v_h(s,r) \exp\left(- \int_r^{\infty} a(s,\tau) d\tau \right) dr \\ &= c \cdot \exp\left(- \int_{x_h}^{s} \lambda_h(\tau) d\tau \right) \int_{\mathbb{R}} \frac{\mu(s,r) e^{-\int_r^{\infty} a(s,\tau) d\tau}}{\alpha_h(s)\sqrt{2\pi}} \exp\left(- \frac{(r-h)^2}{2\alpha_h^2(s)} \right) dr. \end{aligned} \tag{10}$$

We can observe that if a, λ and ψ are known, then for each h fixed, the operator $\mu \mapsto p_h(s, \boldsymbol{\theta}^{\perp})$ is a weighted X–ray transform resembling an attenuated X–ray transform with an extra weight. The approach, here presented, considers observations in multiple heights h for only one angle $\boldsymbol{\theta}$. But, another interesting problem can come out if we additionally consider observations for several angles $\boldsymbol{\theta} \in S^1$, to simultaneously recover μ and the attenuation a (or λ) as in some related works presented in [19, 36, 37, 11].

In the next section, we introduce the measurement operator $\mathcal{P}$ to study the inverse problem related with the reconstruction of μ from the expression (10).

3. Inverse problem

In this section we will summarize all the elements involved in the description of the measurement operator $\mathcal{P}$, we will discuss about the admissible sections of a domain Ω where the model $\mathcal{P}$ is a more adequate description of the phenomena, and we will pose the inverse problems of reconstructing μ as the inversion of the measurement operator $\mathcal{P}$.

3.1. Physical Quantities

In the previous section we considered the following quantities involved in the phenomena,

(i) $\lambda(x,y)$ describing the attenuation for the incident laser inside the domain.

(ii) $\psi(x,y)$ describing the diffusion of the laser as it propagates inside the domain.

(iii) $\mu(x,y)$ the density of fluorescent molecules at each point (x,y) in the domain.

(iv) $a(x,y)$ describing the attenuation of the fluorescent light inside the domain.

(v) c the activation constant, describing the proportion of incident light that excite the fluorophores.

We will assume $\lambda, \mu, a \in C_{\mathrm{pw}}(\overline{\Omega})$ and $\psi \in C^1(\overline{\Omega})$, where C_{pw}, C^1 denote the set of piecewise continuous and continuously differentiable functions, respectively, we assume that these functions vanish outside of $\overline{\Omega}$ and that $\psi > 0$ in $\overline{\Omega}$. Under these conditions all the solutions to the equations in Section 2 exist and are unique (piecewise continuous regularity could be replaced by L^1 regularity). We recall that we are using the notation $\lambda_h(x) := \lambda(x, h)$ and $\psi_h(x) := \psi(x, h)$.

3.2. Admissible domain

It is important to observe that (4) is a solution to equation (3) only under the hypothesis that $\psi_h > 0$. Therefore the model for the incident excitation is not as correct after the laser exits the domain Ω, hence equation (10) describing the fluorescent measurement $p_h(s)$ in pixel s arising from an incident excitation at height h, is more adequate if the segment $[x_h, s] \times \{h\}$ is contained in $\overline{\Omega}$. We will consider this aspect for the theoretical part of this work, which motivates the following definitions.

Definition 1 *(See Figure 4 for an illustration of the following definitions). Let* $\Omega \subset [0, s_1] \times [-y_1, y_1]$ *be an open set with smooth boundary. Recall that for* $h \in [-y_1, y_1]$ *we defined* $x_h = \inf\{x : (x, h) \in \Omega\}$. *For* $s \in [0, s_1]$ *define*

$$\begin{aligned} Y_s &= \{h \in [-y_1, y_1] : x_h \leq s\} \\ s^- &= \inf\{s : Y_s \neq \emptyset\}, \end{aligned}$$

and observe that $Y_s \subset Y_r$ *for* $s < r$. *We say that* $s \in [s^-, s_1]$ *is admissible if* $[x_h, s] \times \{h\} \subset \overline{\Omega}$, *for all* $h \in Y_s$. *We define* s^+ *as the supremum over the admissible* s, *we define* $\underline{y}(s) = \inf(Y_s)$ *and* $\overline{y}(s) = \sup(Y_s)$ *for all* $s \in [s^-, s^+]$, *and we let* $y^- = \underline{y}(s^+), y^+ = \overline{y}(s^+)$. *We define the admissible section of* Ω *as* $\Omega_{\mathrm{ad}} = \{(x, y) \in \Omega : x \leq s^+\}$ *and we also define* $\gamma : Y_{s^+} \to [0, s^+]$ *as* $\gamma(h) := x_h$, i.e. *as the unique smooth function satisfying*

$$\Omega_{\mathrm{ad}} = \{(x, y) : \gamma(y) \leq x \leq s^+\}.$$

If the set Ω *is additionally convex, then* $Y_{s^+} = [y^-, y^+]$, *and if the set* Ω *is convex and oriented properly then* Ω_{ad} *covers half of* Ω, *in the sense that at both boundary points* (s^+, y^-) *and* (s^+, y^+) *the boundary is tangent to an horizontal line (see Figure 5).*

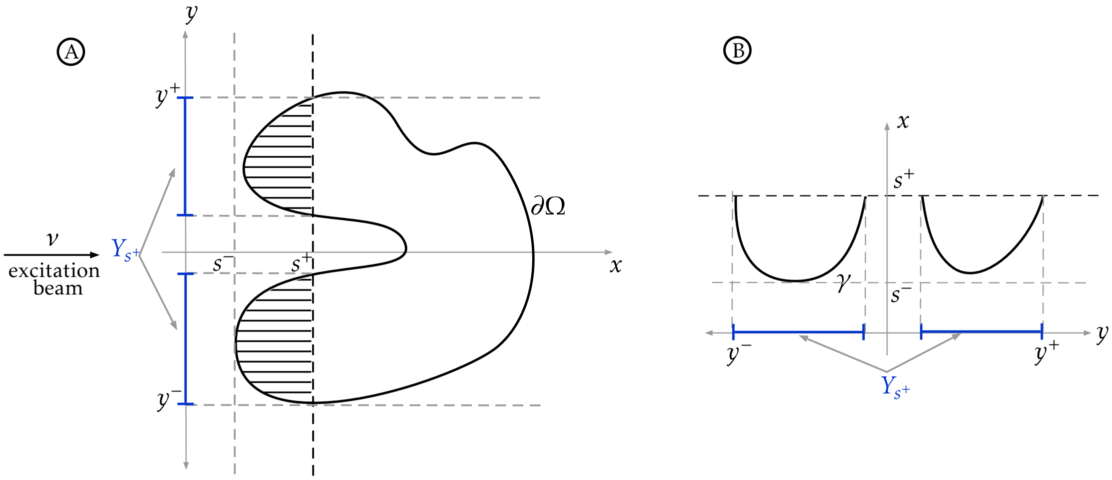

Figure 4: Example of an admisible domain and the corresponding γ function for a generic set Ω. Figure A presents the definition of the quantities s^- and s^+ and the set Y_{s^+}. Figure B shows function γ and its domain Y_{s^+} in the new coordinates.

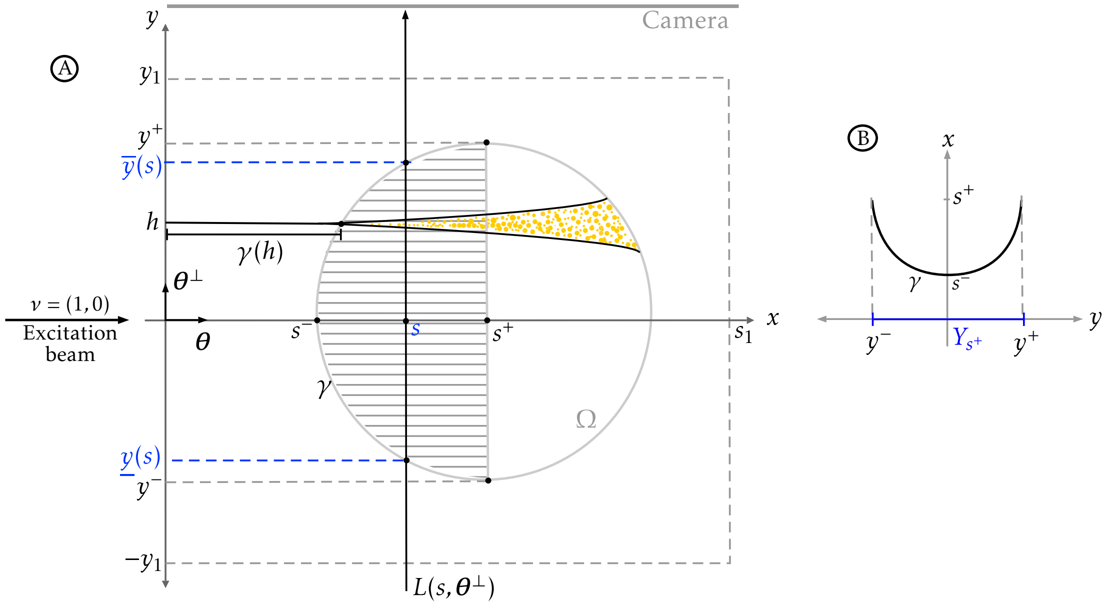

Figure 5: Example of an admissible domain for a convex set Ω. On the left side, in figure A, we present its admissible section Ω_{ad} filled. All variables are defined under this scenario. Figure B, at right, shows the corresponding function γ and its domain Y_{s^+}.

Following the discussion above, we will proceed to the theoretical analysis of the inverse problem considering only the admissible section Ω_{ad} of the domain Ω, even though the proposed model could still be used as an approximate description of the whole phenomena in the full domain Ω. Once we are able to solve the inverse problem on an admissible section, the solution to the inverse problem in the full domain follows in a similar fashion as the merging method suggested in [21]. For the right orientation of the camera, which depends on the geometry of the sample, it is possible to solve the inverse problem in Ω by solving two (or possible more) local problem for admissible regions. This assumes of course the possibility of illuminating the domain from different directions which might be limited by the particular microscope set up. From a numerical point of view, when we leave domain Ω as we are considering that no diffusion is happening (since $\varphi \in C^1(\Omega)$), integration along lines will be just a rough approximation of the real experiment as in the line shown in Figure 5. But if we restrict our analysis to the admissible domain Ω_{ad}, we guarantee that the integrals along $L(x, \boldsymbol{\theta}^\perp)$ after excitation at height y with $(x, y) \in \Omega_{\text{ad}}$ fits the exact value given by the model and not just an approximation. We explain this in Figure 5.

To complete the framework for the theoretical study we require one more condition with respect to the shape of the domain Ω, prescribed in the following definition.

Definition 2 *We will say that a domain Ω is admissible if it satisfies that $\Omega = \Omega_{\text{ad}}$ and if additionally $\gamma \in C^1(Y_s)$ and $\gamma'(\underline{y}(s)) < 0, \forall s \in (s^-, s^+)$.*

3.3. Measurements and Inverse Problem

For the rest of the paper, we will assume that $\Omega = \Omega_{\text{ad}}$ is an admissible domain, in addition to the aforementioned conditions that $\lambda, \mu, a \in C_{\text{pw}}(\overline{\Omega}_{\text{ad}})$, $\psi \in C^1(\overline{\Omega}_{\text{ad}})$, that these functions vanish at (x, h) if $x < x_h$, and that $\psi > 0$ in $\overline{\Omega}_{\text{ad}}$. In terms of the inverse problem we consider that λ, a and ψ are known, while μ is the unknown quantity.

Definition 3 (measurement operator) *We define the measurement operator $\mathcal{P}$ defined on functions $\mu \in C_{\text{pw}}(\overline{\Omega}_{\text{ad}})$ given by (see equation (10))*

$$\mathcal{P}[\mu](s, h) = p_h(s), \quad (s, h) \in \Omega_{ad}.$$

And therefore, the inverse problem consists in recovering μ from the knowledge of $\mathcal{P}[\mu]$, *i.e.*, we want to study the invertibility of the linear operator $\mathcal{P}$.

In next section, we present an injectivity result for the operator $\mathcal{P}$; this will guarantee that $\ker \mathcal{P} = \{0\}$ and consequently if the data $p_h(s)$ is in the range of $\mathcal{P}$, it will uniquely characterize the unknown function μ [3]. In practice, our measurement operator has to be discretized, and the available data contains noise. Hence, this discretized measurement operator is often not injective, but it will be seen as an approximation of

$\mathcal{P}$, which we will prove is injective. We will overcome the ill-posedness generated by noise data in the discretized inverse problem introducing some regularization techniques as is described in Section 7.

4. Injectivity of the measurement operator

For an admissible domain $\Omega_{\rm ad}$ and under the hypotheses described in the previous section, we have the following injectivity result for the operator $\mathcal{P}$.

Theorem 1 *The measurements $\mathcal{P}[\mu]$ uniquely determine the density of fluorophores μ in Ω_{ad}.,* i.e. *if $\mathcal{P}[\mu](s,h) = \mathcal{P}[\nu](s,h)$ for all $(s,h) \in \Omega_{ad}$ then $\mu(x,y) = \nu(x,y)$ for all $(x,y) \in \Omega_{ad}$.*

This results is a direct consequence of a more localized injectivity property of the linear operator $\mathcal{P}$, described in the following theorem.

Theorem 2 *Let $s \in (s^-, s^+)$. If $\mathcal{P}[\mu](s,h) = 0$ for all $h \in Y_s$ then $\mu(s,y) = 0, \forall y \in Y_s$.*

Proof: Let $s \in (s^-, s^+)$ be fixed. Let us recall that for $h \in Y_s$ the measurements take the form (see equations (7) and (10))

$$\mathcal{P}[\mu](s,h) = \exp\left(-\int_{\gamma(h)}^{s} \lambda_h(\tau)d\tau\right) \int_{\mathbb{R}} \frac{c\mu(s,r)e^{-\int_r^\infty a(s,\tau)d\tau}}{\sqrt{2\pi\alpha_h^2(s)}} \exp\left(-\frac{(r-h)^2}{2\alpha_h^2(s)}\right) dr,$$

where

$$\alpha_h^2(s) = \int_{\gamma(h)}^{s} (s-\tau)^2 \psi(\tau,h) d\tau.$$

We observe that by letting

$$f(y) := c\mu(s,y) \exp\left(-\int_y^\infty a(s,\tau)d\tau\right),$$

$$g(h) := \exp\left(\int_{\gamma(h)}^{s} \lambda_h(\tau)d\tau\right) \mathcal{P}[\mu](s,h), \text{ and}$$

$$\sigma(h) := \alpha_h^2(s)/2,$$

then the theorem reduces to show that $f(y) = 0, \forall y \in Y_s$ whenever $g(h) = 0, \forall h \in Y_s$, where

$$g(h) = \int_{\mathbb{R}} \frac{f(r)}{\sqrt{4\pi\sigma(h)}} \exp\left(-\frac{(r-h)^2}{4\sigma(h)}\right) dr. \tag{11}$$

If $U(t,y)$ is the unique solution to the following initial value problem for the heat equation,

$$\begin{cases} (\partial_t - \partial_y^2)U(t,y) = 0, \quad (t,y) \in (0,+\infty)\times\mathbb{R}, \\ U(0,y) = f(y), \text{ if } y \in Y_s, \\ U(0,y) = 0, \text{ if } y \notin Y_s, \\ \lim\limits_{|y|\to\infty} U(t,y) = 0, \forall t > 0, \end{cases} \tag{12}$$

then

$$U(t,y) = \int_{\mathbb{R}} \frac{f(r)}{\sqrt{4\pi t}} \exp\left(-\frac{(r-y)^2}{4t}\right) dr,$$

and

$$g(y) = U(\sigma(y),y), \ \forall y \in Y_s, \quad \text{while} \quad f(y) = U(0,y), \ \forall y \in Y_s.$$

Let $\Gamma := \{(\sigma(y),y) : y \in Y_s\} \cup \{(0,y) : y \notin Y_s\}$. Since $g(y) = 0, \forall y \in Y_s$ if and only if $U|_\Gamma = 0$, then we can recast our problem as the problem of proving that

$$U|_\Gamma = 0 \text{ implies } U(0,y) = 0, \ \forall y \in Y_s.$$

This is exactly what Theorem 3 in the following section shows. But to use Theorem 3 we need to check that Γ satisfies the required conditions, which reduces to prove the following

(i) $\sigma : Y_s \to \mathbb{R}$ is C^1.

(ii) $\sigma(y) = 0$ if $y \in \partial Y_s$.

(iii) $\sigma'(y) = 0$ whenever $\sigma(y) = 0$.

(iv) There exists $\delta > 0$ such that $\sigma'(y) > 0$ for $y \in (\underline{y}(s), \underline{y}(s) + \delta)$.

Let us prove this four points. Recall that for $y \in Y_s$

$$\sigma(y) = \frac{1}{2}\int_{\gamma(y)}^{s} (s-\tau)^2 \psi(\tau,y)d\tau, \tag{13}$$

therefore

$$\sigma'(y) = -\frac{1}{2}\gamma'(y)(s-\gamma(y))^2\psi(\gamma(y),y) + \frac{1}{2}\int_{\gamma(y)}^{s}(s-\tau)^2\frac{\partial\psi}{\partial y}(\tau,y)d\tau. \tag{14}$$

The hypotheses on the regularity of γ and ψ clearly imply that $\sigma \in C^1(Y_s)$ and therefore (i) is satisfied. Property (ii) follows from the equation (13) and the fact that if $y \in \partial Y_s$ then $\gamma(y) = s$. In order to check (iii) let us recall that $\psi > 0$ in Ω, therefore $\sigma(y) = 0$ only if $\gamma(y) = s$ (see equation (13)), in which case equation (14) implies $\sigma'(y) = 0$. To establish (iv), we observe that if $m = \inf_{(x,y)\in\overline{\Omega}} |\psi(x,y)| > 0$ and $M = \sup_{(x,y)} |\partial\psi/\partial y(x,y)|$ then from equation (14)

$$\frac{2\sigma'(y)}{(s-\gamma(y))^2} \geq \Big[-\gamma'(y)m - \frac{1}{3}(s-\gamma(y))M \Big] \overset{y\to\underline{y}(s)}{\longrightarrow} -\gamma'(\underline{y}(s))m,$$

since Ω is admissible, $\gamma'(\underline{y}(s)) < 0$ and therefore $\sigma'(y) > 0$ for $y \in (\underline{y}(s), \underline{y}(s) + \delta]$, for some $\delta > 0$. □

5. A uniqueness result for the heat equation

The purpose of this section is to prove the next result.

Theorem 3 *Let $\sigma(y) \in C^1_c(\mathbb{R})$ and denote $\Gamma = \{(t,y) \in \mathbb{R}^2 : t = \sigma(y)\}$. Let*

$$\underline{y} = \inf(\operatorname{supp}\sigma), \quad \overline{y} = \sup(\operatorname{supp}\sigma)$$

and assume there is $\delta > 0$ so that $\sigma'(y) > 0$ in $(\underline{y}, \underline{y} + \delta)$. If $U(t,y)$ is a solution to the heat equation

$$\begin{aligned}(\partial_t - \partial_y^2)U(t,y) = 0, \quad (t,y) \in (0,+\infty)\times\mathbb{R},\\ U(t,y) \to 0 \text{ as } |y| \to \infty, \ \forall t > 0,\end{aligned}$$

satisfying $\operatorname{supp} U|_{t=0} \subset \operatorname{supp}\sigma$ and $U|_\Gamma = 0$, then $U = 0$ everywhere in $(0,+\infty)\times\mathbb{R}$. In particular $U(0,y) = \lim_{t\to 0^+} U(t,y) = 0, \forall y \in \mathbb{R}$.

Proof: Let $T = \sigma(\underline{y}+\delta)$, by hypothesis the restriction of σ to the interval $(\underline{y}, \underline{y}+\delta)$ has an inverse $\rho(t) = \sigma^{-1}(t) \in C^1(0,T) \cap C[0,T]$, and since $\sigma(\underline{y}) = 0$ then $\rho(0) = \underline{y}$. Then we can parameterize the section of Γ immediately to the right of $(\underline{y}, 0)$ as $\{(\rho(t), t) : 0 \leq t \leq T\}$ (see Figure 6). Let us define the following one–sided exterior energy

$$I(t) := \frac{1}{2}\int_{-\infty}^{\rho(t)} |U(t,y)|^2 dy, \quad t \in [0,T),$$

and notice that for all $t \in (0,T)$

$$\frac{d}{dt}I(t) = \frac{1}{2}|U(\rho(t),t)|^2 \frac{d}{dt}\rho(t) + \int_{-\infty}^{\rho(t)} U(t,y)\partial_t U(t,y) dy,$$

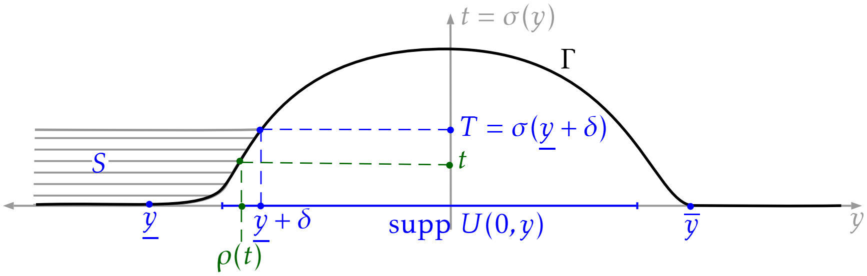

Figure 6: Curve Γ in variables $(y, t) \in \mathbb{R} \times (0, +\infty)$. The filled zone $\{(y, t)\colon 0 \le t < T,\ y < \rho(t)\}$ has been denoted by S. The assumption that $\operatorname{supp} U|_{t=0} \subset \operatorname{supp} \sigma$ is also represented, since $\underline{y} = \inf(\operatorname{supp} \sigma)$ and $\overline{y} = \sup(\operatorname{supp} \sigma)$.

and the first term in the sum vanishes since $U|_\Gamma = 0$. On the other hand, since U solves the heat equation and integrating by parts,

$$\begin{aligned}\int_{-\infty}^{\rho(t)} U(t, y)\partial_t U(t, y) dy &= \int_{-\infty}^{\rho(t)} U(t, y)\partial_y^2 U(t, y) dy \\ &= U(t, \cdot)\partial_y U(t, \cdot)\Big|_{-\infty}^{\rho(t)} - \int_{-\infty}^{\rho(t)} |\partial_y U(t, y)|^2 dy,\end{aligned}$$

and again the first term in the sum vanishes since $U|_\Gamma = 0$. Therefore

$$\frac{d}{dt} I(t) = -\int_{-\infty}^{\rho(t)} |\partial_y U(t, y)|^2 dy \le 0, \quad \forall t \in [0, T),$$

and $I(t)$ is a nonnegative decreasing function. But $\operatorname{supp} U(0, y) \subset \operatorname{supp} \sigma$, implying that $I(0) = 0$ and concluding that $I(t) = 0$ for all $t \in [0, T)$. It follows that

$$U(t, y) = 0, \quad \forall t \in [0, T), \forall y < \rho(t),$$

and from classical unique continuation results for parabolic equations (see for instance [26]) we deduce that U must vanish in the whole upper-half plane.

□

In the next sections, we present the numerical implementation of the direct and inverse problems.

6. Discrete direct and inverse problems

The main objective of this and next sections is to present a numerical analysis and solution of the direct and inverse problems. This will allow us to bear out that the diffusion and artifacts, observed during the traditional acquisition process, can be described by the proposed model.

6.1. Direct model

Here, we present how to simulate our data set using the proposed forward operator $\mathcal{P}$. Given the fluorescence density μ in a given domain Ω, we are able to compute the value of $p_h(s)$ for all s thanks to the expression (10).

The density of fluophores μ and the two cases of attenuation λ that we will consider in the experiments are presented in Figure 7. The variable attenuation is proportional to the fluorophore density plus a constant value which represents the medium where the object is submerged. We assume that the attenuation of the fluorescence stage a satisfies the relation $a = \hat{c} \cdot \lambda$. We choose a parameter $\hat{c}$ so that the diffusion effect got in the numerical experiments remains close to the one observed in the real data. Here, we also assume that the diffusion term ψ_h is proportional to the attenuation λ_h, *i.e.* $\psi_h = \tilde{c} \cdot \lambda_h$. For all the experiments we set this constant in $\tilde{c} = 0.6$. Additionally, recalling that $w_h = c \cdot \mu \cdot v_h$, represents the amount of fluorescent molecules that is activated after the excitation process, we took $c = 1$ throughout the experiments.

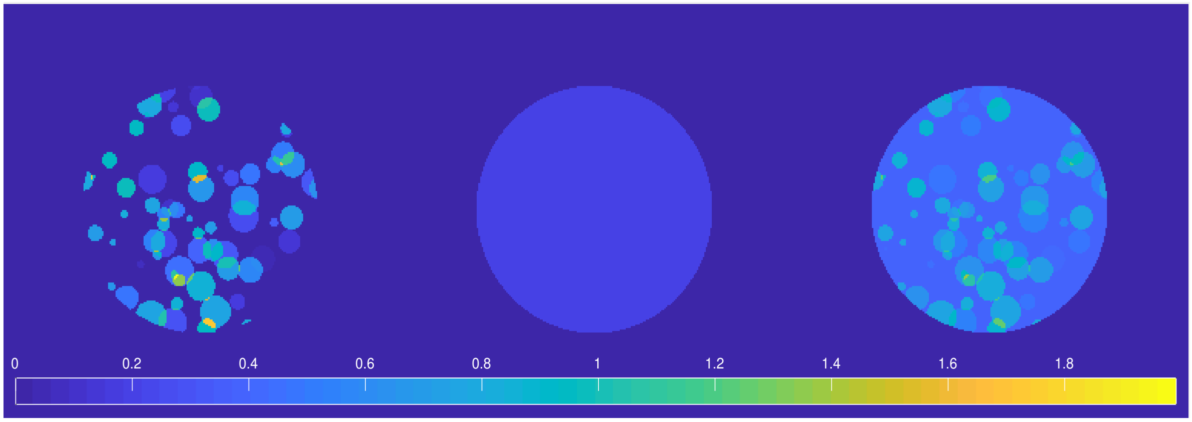

Figure 7: From left to right: fluorophore density distribution (μ), constant and variable attenuation (λ) for the excitation stage.

For all experiments, we work over the domain $\Omega = [0, 2] \times [-1, 1]$ and with images of size $N \times N$ with $N = 257$. The discretization step is given by $\tau = 2/(N + 1)$ in x and y axes. We start by calculating the values $v_h(x, y)$ over Ω for a discretized set of excitations points along the interval $[-1, 1]$. We take N heights of excitations with step size τ. The excitation points are considered in two directions: left and right, since the support of our object is a circle (as shown in Figure 7) by the Definition 1, two directions are needed to guarantee the uniqueness of our solution in the whole domain.

Then the total amount of excitation points is $2N$.

The discretization of equation (6) is straightforward if we approximate the integrals of λ_h as finite sums of its pixel intensities, since we are representing λ_h as an image of size $N \times N$. The same is considered for the integrals of ψ_h in expression (5).

Figure 8 presents a single simulation of $v_h(x, y)$ when the excitation point occurs at $h = -0.1406$, from both directions (left and right). We also included a visualization of the function w_h.

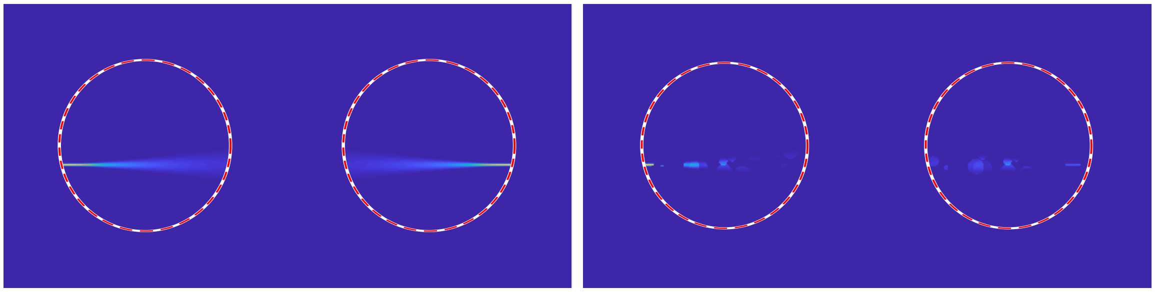

Figure 8: The left image corresponds to the v_h image after illuminating at $h = -0.1406$ from left and right, respectively. In the second image, we show the function w_h for the same height. We included the support of our object in broken red lines for visualization purposes.

To achieve the discretization of the equation (10), we define the set of discrete values of h as $\{h_l\}$ for $l = 1, \ldots, 2N$ and analogously, for s we consider $\{s_k\}$ for $k = 1, \ldots, N$. Additionally, as images a and μ are seen as matrices, we index them as a_{ij} and μ_{ij} for $i, j = 1, \ldots, N$. Finally, a line of observation is defined by the distance s_k, and we denote it by L_k.

In Figure 9, we describe all the discrete variables that we have introduced. The filled pixels represent an example of the discretized function v_h when the excitation occurs at the point h_l of our discrete domain. We denote by v_{ijl} the value of v_h in the pixel indexed by (i, j) when $h = h_l$. We use the Kronecker delta to determine if a line L_k is intersecting a pixel (i, j), this happens when we are at pixels where $j = k$, then:

$$\delta_{jk} = \begin{cases} 1, & \text{if } j = k, \\ 0, & \text{otherwise.} \end{cases}$$

Then $\mathcal{P}[\mu](s_k, h_l) = p_{h_l}(s_k)$ is calculated as:

$$\mathcal{P}[\mu](s_k, h_l) = c \sum_{i,j=1}^{N} \delta_{jk} \mu_{ij} v_{ijl} \exp\left(-D_{ik}(a)\right), \tag{15}$$

$$= c \sum_{i=1}^{N} \mu_{ik} v_{ikl} \exp\left(-D_{ik}(a)\right), \tag{16}$$

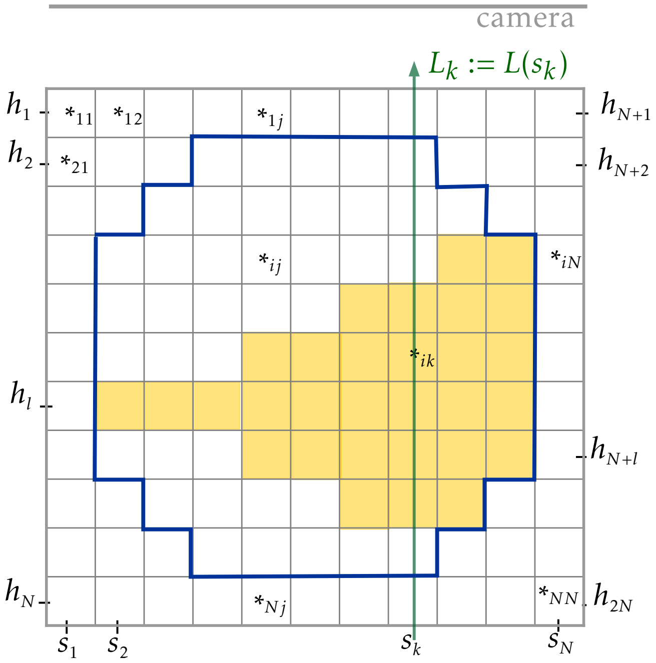

Figure 9: Discretization of the image and the variables used in the AtRt.

where

$$D_{ik}(a) = \sum_{z=1}^{i} a_{zk}$$

is interpreted as partial sums along the columns of the attenuation a.

Under this discretization, our set of measurements is of size $2N^2$, for all (s_k, h_l) with two–side excitations (we highlight that the density μ has N^2 pixels that is the amount of unknowns of our problem). In Figure 1, the first two images represent the matrix of measurements obtained from left and right excitations, respectively. In the third one, the fused image (as in [20] is presented to compare it with the reconstruction obtained by the proposed model.

In Figure 10, we compare the fused image and the ground truth density μ under the same scale of values. This figure shows that the density that is measured by the camera is not as good and need to be corrected in the central zone, which was our initial motivation. In the next section, we study the numerical inversion of the proposed inverse problem and present possible improvements that can be obtained through our approach.

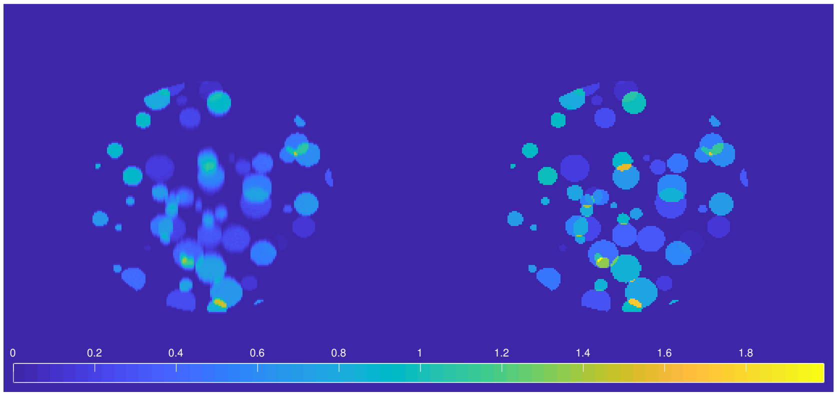

Figure 10: The fused image (see Figure 1) of measurements (left) compared to the ground truth density (right).

6.2. Inverse model

We take advantage of the linearity of the operator $\mathcal{P}$ described in Definition 3, to represent the solution of our discretized inverse problem as the solution of a linear system of the form:

$$A\boldsymbol{\mu} = b, \qquad A \in \mathbb{R}^{m\times n},\ b \in \mathbb{R}^m,\ \boldsymbol{\mu} \in \mathbb{R}^n. \tag{17}$$

To build the matrix A associated to our problem, we have to do small changes to the previous discretization. We just reorder (μ_{ij}) as a vector $\boldsymbol{\mu}$ of size $N^2 \times 1$ as shown in the expression below. We use the variable z to index pixels, so $z = 1, \dots, N^2$. The same is needed for $\boldsymbol{v}_l := (v_{ijl})$:

$$\boldsymbol{\mu} = (\mu_z) = \begin{bmatrix} \mu_{11} \\ \mu_{21} \\ \mu_{31} \\ \vdots \\ \mu_{NN} \end{bmatrix}, \qquad \boldsymbol{v}_l = (v_{zl}) = \begin{bmatrix} v_{11l} \\ v_{21l} \\ v_{31l} \\ \vdots \\ v_{NNl} \end{bmatrix}, \ \forall l = 1, \dots, 2N.$$

Equivalent to the Kronecker delta we introduce a matrix that can tell us the whole information about the intersections between lines L_k and a pixel z. For a fixed pixel z and distance s_k, we define

$$w_{zk} = \begin{cases} 1, & \text{if line } L_k \text{ crosses the pixel } z, \\ 0, & \text{otherwise.} \end{cases}$$

Then, we can write a vector $\boldsymbol{w}_k$ of size $N^2 \times 1$, as follows:

$$\boldsymbol{w}_k = \Big[w_{1k},\ w_{2k},\ w_{3k},\ \cdots,\ w_{N^2k} \Big]^\top .$$

And defining $\boldsymbol{W}_{kl} = \boldsymbol{v}_l \odot \boldsymbol{w}_k$, where $\odot$ represents the Hadamard or point–wise product. The only part that needs to be written as a vector in expression (15) is the exponential term, for this, we define a matrix (D_z) as the cumulative sums of the attenuation matrix a in the direction of the camera. The farther a pixel is from the camera, the greater its accumulated value. As before, we rewrite this matrix as a $(N^2 \times 1)$–vector, that we denote by $\boldsymbol{D}$:

$$\boldsymbol{D} = \Big[D_1,\ D_2,\ D_3,\ \cdots,\ D_{N^2} \Big]^\top .$$

Now, for each k and l, we write a row of our final matrix A as:

$$\boldsymbol{a}_{kl} = \boldsymbol{W}_{kl} \odot \exp(-\boldsymbol{D}),$$

where $\exp(-\boldsymbol{D})$ is understood as the exponential of each component of $\boldsymbol{D}$. Then varying k and l, we built A of size $m \times n$, with $m = 2N^2$ and $n = N^2$. To build the vector of measurements b, as we obtain our set of observations (as the first two images presented in Figure 1), we just need to reshape them as a column vector taking row by row and transposing them. The shape of the matrix A and vector b are:

$$A = \left[\begin{array}{cccc|cccc|c|cccc} \boldsymbol{a}_{11} & \boldsymbol{a}_{21} & \cdots & \boldsymbol{a}_{N1} & \boldsymbol{a}_{12} & \boldsymbol{a}_{22} & \cdots & \boldsymbol{a}_{N2} & \cdots & \boldsymbol{a}_{1,2N} & \boldsymbol{a}_{2,2N} & \cdots & \boldsymbol{a}_{N,2N} \end{array} \right]^\top ,$$

$$b = \left[\begin{array}{cccc|cccc|c|cccc} b_{11} & b_{21} & \cdots & b_{N1} & b_{12} & b_{22} & \cdots & b_{N2} & \cdots & b_{1,2N} & b_{2,2N} & \cdots & b_{N,2N} \end{array} \right]^\top .$$

6.2.1. Solution of the linear system. As the matrix A is sparse and large, a factorization process to solve (17) could be impossible or computationally expensive. For this reason, the use of iterative methods is highly desirable to solve this type of linear systems.

Additionally, we consider that our measurements (represented by the right-hand vector b) are corrupted by unknown vector of noise $\varepsilon \in \mathbb{R}^m$, as is usual in the real cases. For the different iterative algorithms that we will present, we assume that at least the norm $\delta := \|\varepsilon\|$ is known.

Then, due to the ill–posedness produced by the presence of noise and the possible ill-conditioned matrix A, a *regularization process* can be used to overcome these issues [9].

The regularized minimization problem associated to the solution of the linear system (17) is:

$$\mu = \arg\min_{x \in \mathbb{R}^m} \left\{ \frac{1}{2}\|Ax - b\|_2^2 + \lambda \mathcal{R}(x) \right\} \tag{18}$$

where the data–fit term $\|Ax - b\|_2^2$ forces the problem to find x that remains close to the given data b, and the regularizer term $\mathcal{R}$ is chosen to overcome the particular requirements of each problem. An alternative way to include the regularization is to apply an iterative method directly on the data–fit term and use the number of iterations as stop criteria when semi-convergence is achieved. The general principle of the semi–convergence is to obtain a desired approximation before the noise starts to show up in the current solution [17, Chapter 6]. The algorithms used to solve our problem consider these two possible approaches.

In the next section, we briefly describe the algorithms that are used to solve our linear system and hence, the inverse problem. We have implemented the discretization of our problem in MATLAB and we solve the linear system using the IR TOOLS which are detailed in [13].

7. Numerical results

In this part, we propose to solve our discrete inverse problem using two different minimization approaches, that we denote by (P1) and (P2) and are defining as follows:

$$\begin{cases} \underset{x}{\text{minimize}} & \|Ax - b\|_2^2 \\ \text{subject to} & x \in \mathcal{C} \end{cases} \tag{P1}$$

$$\begin{cases} \underset{x}{\text{minimize}} & \|Ax - b\|_2^2 + \lambda\, \mathrm{TV}(x) \\ \text{subject to} & x \geq 0 \end{cases} \tag{P2}$$

The Problem (P1) is related to the *semi–convergence* case, where the regularization will be included within the iterations of the optimization algorithms. We will compare the results obtained by five different algorithms: the *Modified residual norm steepest descent method* [27] (`mrnsd`), the *Flexible CGLS method* [15] (`nnfcgls`), *Simultaneous algebraic reconstruction technique* [18] (`sart`) and the *Fast Iterative Shrinkage-Thresholding Algorithm* (`fista`) [6] (that solves the Tikhonov problem with box constraints when the parameter $\lambda = 0$, a penalized version is also available if $\lambda \neq 0$ but we are not considering this case).

The problem (P2) has the shape of (18) where we have considered the *total variation*

(TV, [34]) as our regularizer $\mathcal{R}$. To solve it, we use a particular case of the *Projected-restarted iteration method* (PRI) [9] which incorporates a heuristic TV penalization term [14]. As in [13], we denote this method by (`htv`).

7.1. Simulated noise measurements

To avoid *inverse crime* in our reconstructions, we add noise to our simulated measurements. For this, we consider an scaling factor β to generate a poisson distributed noise (since this random variable returns normal values, it is necessary to amplify the signal). The factor β controls the level of noise, *i.e.*, if β takes large values, we will get lower intensity images and therefore higher poisson noise [25]. Accordingly, each pixel value p is replaced by a draw $\beta \cdot \mathrm{Pois}\left(\frac{p}{\beta}\right)$ as in [25, eq. 2].

Examples 1 and 2 described below are implemented with values $\beta = 0.01$ and $\beta = 0.001$, respectively.

7.2. Stop criteria

In this IR TOOLS package, all algorithms mentioned above used the *discrepancy principle* to stop in the *best* iteration. For the algorithms `sart`, `fista`, `mrnsd` and `nnfcgls`, this means that the algorithms stop as soon as the relative norm of the residual $b - Ax^{(k)}$ is sufficiently small, typically of the same size as the norm of the noise ε, *i.e.* when

$$\frac{\|b - Ax^{(k)}\|_2}{\|b\|_2} \leq \eta \cdot \mathtt{NoiseLevel}$$

where η is a “safety factor” slightly larger than 1, and `NoiseLevel` is the relative noise $\|\varepsilon\|_2/\|b\|_2$.

For the algorithm `htv` that is a PRI method with inner–outer iterations, the discrepancy principle is used to stop the inner iterations, whilst the outer iterations are stopped when $\|x^{(k)}\|$, $\|\,\mathrm{TV}(x^{(k)})\|_2$ or the value of the regularizer parameter λ, becomes stable.

7.3. Initialization

We use the fused image of measurements (see Figure 1) as initial value $x^{(0)}$ (see Figure 10), this initializing helps to improve the speed of the algorithms and reduce the number of iterations.

When the parameter η is needed, we considered $\eta = 1.01$. Additionally, since we simulate the data as shown in Section 6, we have at our disposal the true value of the unknown image μ which is included in the algorithm to calculate the relative error.

Example 1:

In this first simulated example, we consider that the attenuations λ and a are constant over the domain Ω. This means that we are only considering the effects of the medium where our object of interest in submerged. In Table 1, we present the results in terms of number of (outer) iterations, time of execution, the relative error (NRE) and the structural similarity coefficient (SSIM, [39]) between the reference (true) density and the reconstruction. In this example, all the algorithms present a quantitative improvement compared to the values of the fused image. The `htv` method gives the smallest NRE value (0.139%) and `fista` the highest value of the SSIM (0.98439). In Figure 12, we can visually compare the different results.

Table 1: Number of iterations, execution time, relative error and SSIM for the different algorithms when attenuation is assume to be known and constant. The "fused image" row corresponds to the third image in Figure 1, which has been perturbed by noise.

Algorithm	iterations	time (s)	$\|x - x^{(k)}\|_2 / \|x\|_2$	SSIM
`fused image`	$--$	$--$	0.1637	0.96402
`fista`	31	4.8129	0.15077	**0.98439**
`htv`	34	1.2496	**0.13914**	0.98349
`mrnsd`	150	2.8388	0.14965	0.98278
`nnfcgls`	106	3.7828	0.14001	0.98383
`sart`	10	1.9969	0.15856	0.98305

$^*x$ is the truth solution.

In Figure 13, we draw the profiles of the reconstructions along $x = 1$ in order to observe the improvements reached in the central region of the image.

Example 2:

In this case, the simulated measurements are generated using variables attenuations λ and a, in order to include some attenuation effects produced by the presence of the fluorescent molecules. However, as in more real cases, the attenuation could be also unknown, we propose to reconstruct the density μ with a constant attenuation a which could be experimentally determined. In our case, we take $a = 1.1$ over Ω. We have included Poisson Noise with `NoiseLevel` $= 0.01$. The results are presented as before in

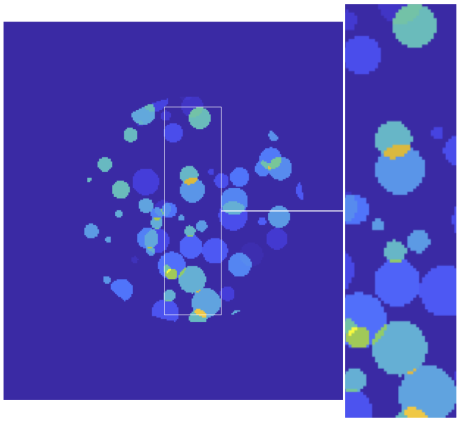

Figure 11: True simulated density, with zoomed zone to visual comparisons.

Figures 14–15 and Table 2. The values of the `nnfcgls` and `sart` methods are slightly better than the other algorithms, but all of them improve the fused image values.

We do not focus on which algorithm is better; we are just interested in the improvements observed in the proposed reconstruction independently of the selection of the optimization algorithm.

Table 2: Number of iterations, execution time, relative error and SSIM for the different algorithms when the attenuation is variable but is considered as constant during the reconstruction. The "fused image" row corresponds to the third image in Figure 1, which has been perturbed by poisson noise.

Algorithm	iterations	time (s)	$\|x - x^{(k)}\|_2 / \|x\|_2$	SSIM
`fused image`	$--$	$--$	0.40466	0.92454
`fista`	29	5.3721	0.29567	0.95875
`htv`	41	2.0133	0.26267	0.96326
`mrnsd`	> 2000	27.976	0.24255	0.97345
`nnfcgls`	> 2000	96.577	**0.22798**	0.97695
`sart`	> 2000	45.802	0.22783	**0.97994**

$^*x$ is the truth solution, the symbol $>$ means stops with a maximum number of iterations.

In Figure 15, we draw the profiles of the reconstructions along $x = 1$ as before. Here we observe that the assumption of the attenuation is constant implies in some parts a underestimation of the true value. This will depend directly from the constant value that we choose for a.

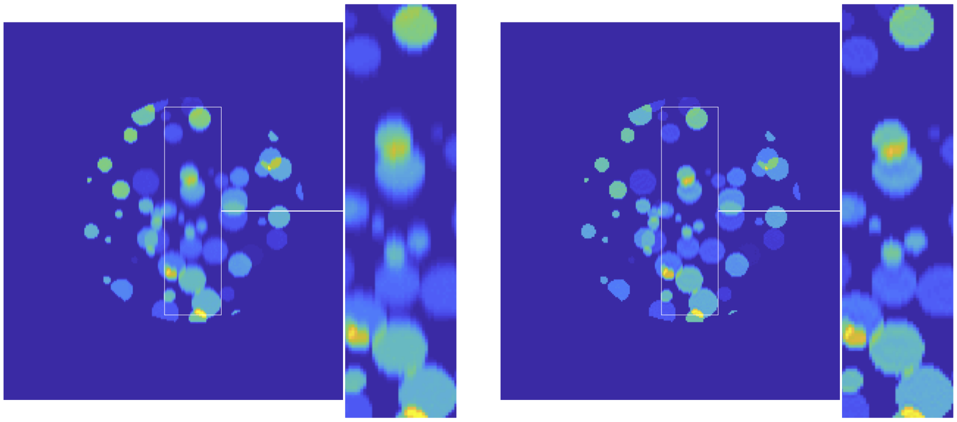

(a) Noise measurements **(b)** fista

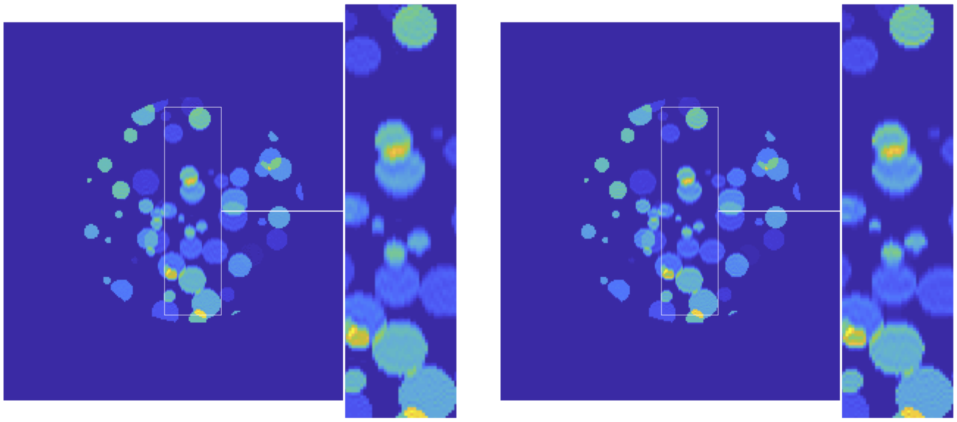

(c) htv **(d)** mrnsd

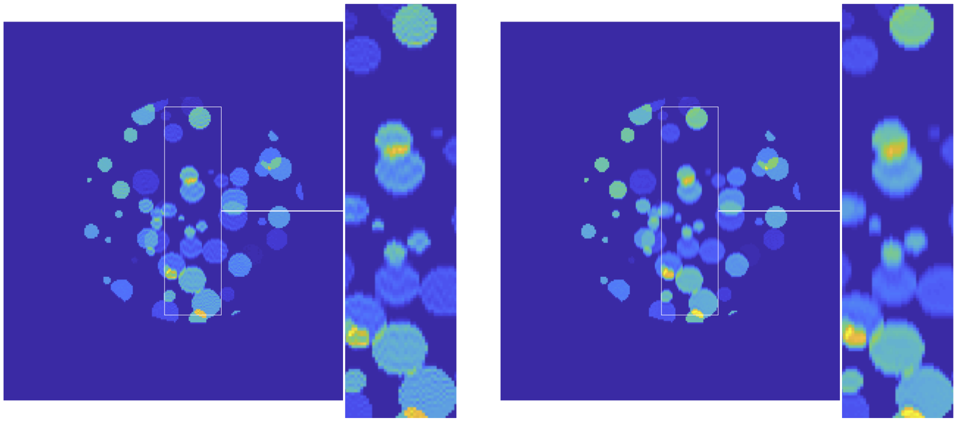

(e) nnfcgls **(f)** sart

Figure 12: For Example 1: zoomed images to visualize the difference between the reconstructions.

8. Conclusions and outlook

We presented a novel mathematical model for the Light Sheet Fluorescence Microscopy. To our best knowledge, this is the first approach in this direction and is an initial step in

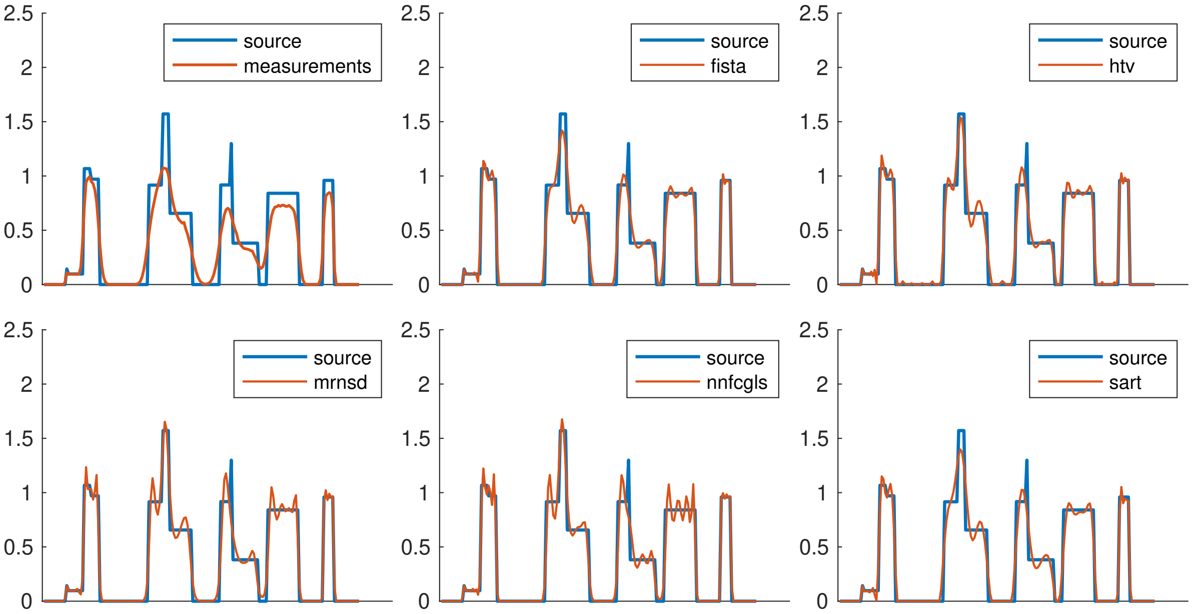

Figure 13: For Example 1: Profiles of reconstruction at $x = 1$ that corresponds to the column 129 of the images.

trying to understand and tackle some of the issues observed in LSFM. This work shows that by considering the acquisition of the density μ as an inverse problem a better reconstruction can be obtained, compared to the traditional merging method that is currently used.

From the theoretical point of view, we presented a uniqueness result for the proposed inverse problem, by reducing it to the recovery of the initial condition in a heat equation with measurements in a space–time curve. The stability in the reconstruction of μ is not considered in this article. However, due to the clear link between the microscopy inverse problem and backward heat propagation the former is expected to be severely ill-posed. The question then is whether Logarithmic stability is the optimal result or if it is possible to obtain a Hölder-type inequality, this kind of result would also open the door to obtain stability results for more physically complete models. This type of question are expected to be addressed in future works.

Additional future work also includes the extension of these results to the three dimensional case, where some extra assumptions might be necessary and we would need to discuss a light-sheet illumination or a beam illumination as the natural extension of the technique presented here.

Questions about a simultaneous reconstruction are also open. For example, about the possibility of recovering the density and the attenuation (either in the illumination or

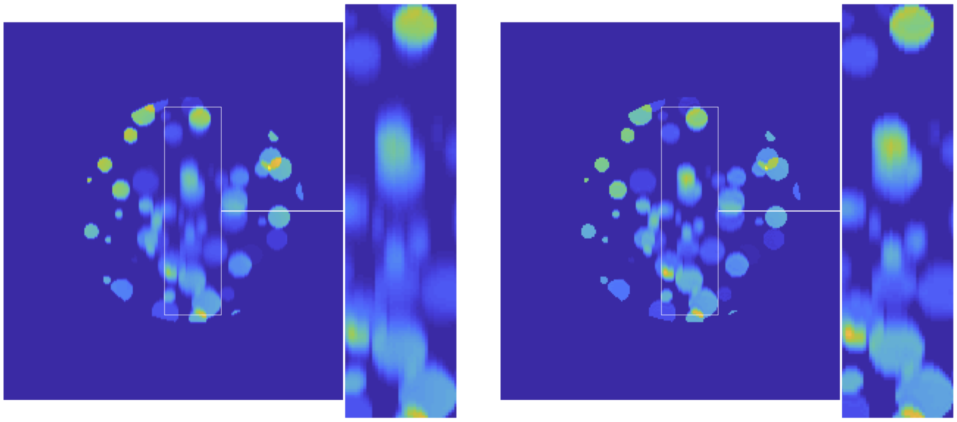

(a) Noise measurements **(b)** fista

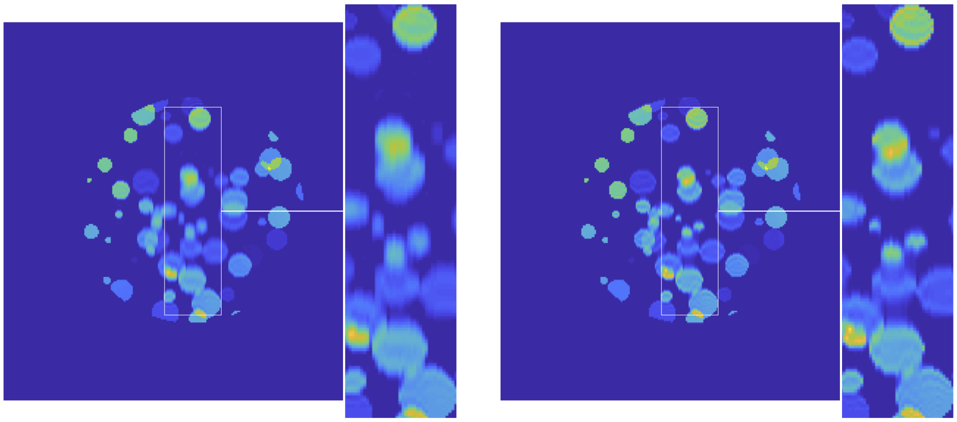

(c) htv **(d)** mrnsd

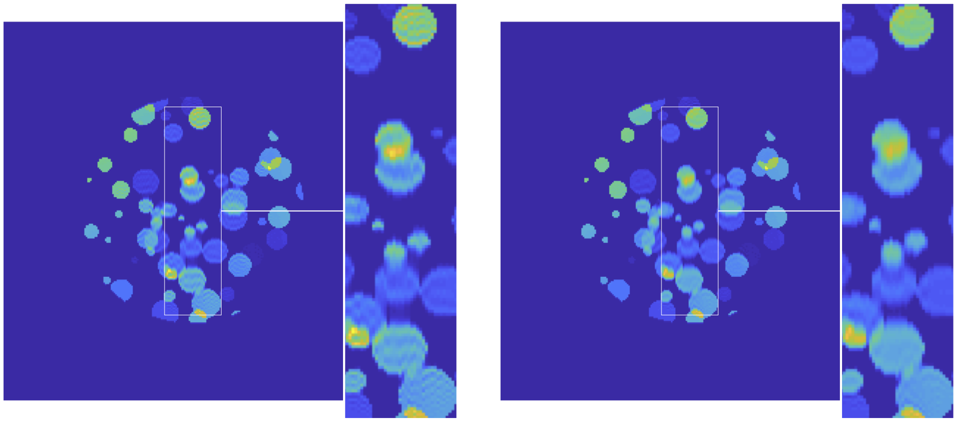

(e) nnfcgls **(f)** sart

Figure 14: For Example 2: zoomed images to visualize the difference between the reconstructions. The images are re-scaled to the range of the ground truth density.

fluorescence) at the same time, by considering additional measurements when rotating the object in multiple directions.

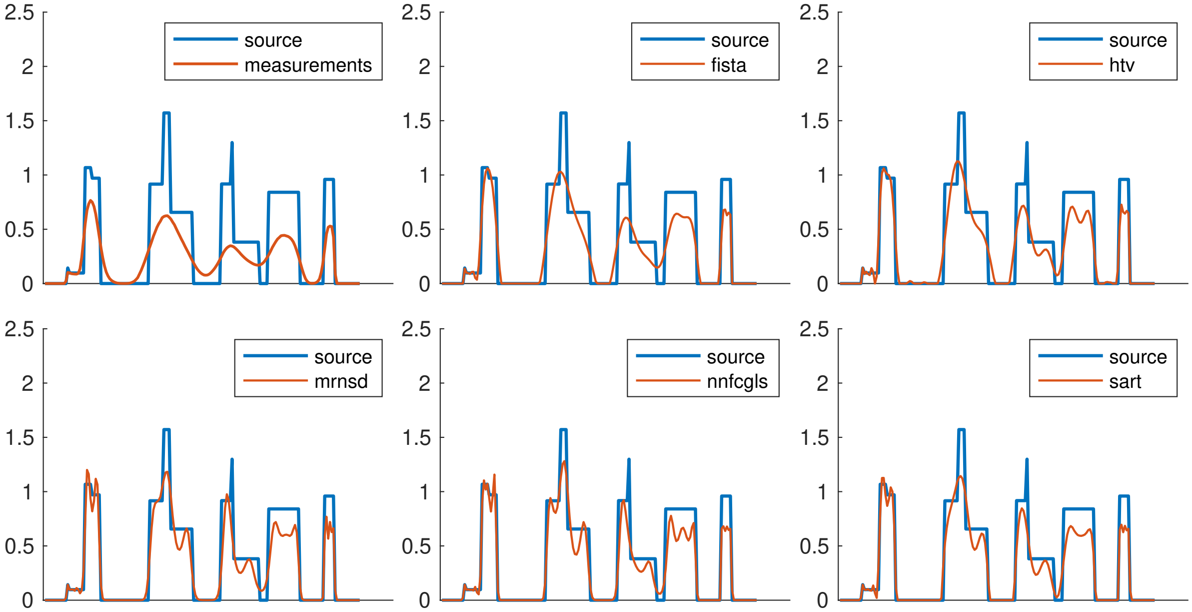

Figure 15: For Example 2: Profiles of reconstruction at $x = 1$ that corresponds to the column 129 of the images.

A more ambitious extension of this work would be to consider more complete and less simplified physics for the illumination and fluorescence stages. In this paper we are heavily reliant in the explicit solution of the Fermi pencil beam equation, which makes it very challenging to extend our results to other illumination models. We are also considering a perfect collimation of the fluorescence measurement and different collimation schemes would give rise to other difficulties. Another ambitious extension of this work would be to include the stochastic nature of the fluorescence stage, which would require an MLEM or similar reconstruction techniques to be considered.

Acknowledgments

E.C. was partially funded by CONICYT-PCHA/Doctorado Nacional/2016-21161721 grant, by SENESCYT/Convocatoria2015 and Project UCH-1566 from the Department of Mathematical Engineering at Universidad de Chile.

A.O. was partially funded by CONICYT grant Fondecyt #1191903, CONICYT Basal Program PFB-03 (AFB170001) and MathAmsud 18-MATH-04 and CONICYT/FONDAP/15110009.

M.C. was partially funded by CONICYT grant Fondecyt #1191903 and M.C. thanks Boğaziçi University, Istanbul, Turkey, as part of this work was completed as a visiting researcher at the institution.

S.H. and V.C. are part of SCIAN-Lab funded by Fondecyt #1181823, EQM140119, CONICYT (PIA ACT 1402), CENS CORFO (16CTTS-66390) and BNI (ICM P09-015-F). SCIAN-Lab is a selected member of the German-Chilean Center of Excellence Initiative (DAAD 57220037 and 57168868). V.C. is also partially funded by CONICYT grant Fondecyt #11170475.

B.P. was partially funded by ONR grant N00014-17-1-2096.

We acknowledge M.D. Miguel Concha for providing us with light-sheet microscopy data (funded by Fondequip EQM130051).

References

[1] Alison Abbott. Cell culture: biology's new dimension, 2003.

[2] Guillaume Bal. Inverse transport theory and applications. *Inverse Problems*, 25(5):053001, 2009.

[3] Guillaume Bal. *Introduction to inverse problems*. 2019.

[4] Guillaume Bal and Alexandre Jollivet. Combined source and attenuation reconstructions in spect. *Tomography and Inverse Transport Theory, Contemp. Math*, 559:13–27, 2011.

[5] Guillaume Bal and Alexandru Tamasan. Inverse source problems in transport equations. *SIAM Journal on Mathematical Analysis*, 39(1):57–76, 2007.

[6] Amir Beck and Marc Teboulle. A fast iterative shrinkage-thresholding algorithm for linear inverse problems. *SIAM journal on imaging sciences*, 2(1):183–202, 2009.

[7] Christoph Börgers and Edward W Larsen. Asymptotic derivation of the fermi pencil-beam approximation. *Nuclear science and engineering*, 123(3):343–357, 1996.

[8] Christoph Börgers and Edward W Larsen. On the accuracy of the fokker–planck and fermi pencil beam equations for charged particle transport. *Medical Physics*, 23(10):1749–1759, 1996.

[9] D Calvetti, G Landi, L Reichel, and F Sgallari. Non-negativity and iterative methods for ill-posed problems. *Inverse Problems*, 20(6):1747, 2004.

[10] Bi-Chang Chen, Wesley R Legant, Kai Wang, Lin Shao, Daniel E Milkie, Michael W Davidson, Chris Janetopoulos, Xufeng S Wu, John A Hammer, Zhe Liu, et al. Lattice light-sheet microscopy: imaging molecules to embryos at high spatiotemporal resolution. *Science*, 346(6208):1257998, 2014.

[11] Matias Courdurier, Francois Monard, Axel Osses, and Francisco Romero. Simultaneous source and attenuation reconstruction in spect using ballistic and single scattering data. *Inverse Problems*, 31(9):095002, 2015.

[12] Leonard Eyges. Multiple scattering with energy loss. *Physical Review*, 74(10):1534, 1948.

[13] Silvia Gazzola, Per Christian Hansen, and James G Nagy. Ir tools: a matlab package of iterative regularization methods and large-scale test problems. *Numerical Algorithms*, 81(3):773–811, 2019.

[14] Silvia Gazzola and James G Nagy. Generalized arnoldi–tikhonov method for sparse reconstruction. *SIAM Journal on Scientific Computing*, 36(2):B225–B247, 2014.

[15] Silvia Gazzola and Yves Wiaux. Fast nonnegative least squares through flexible krylov subspaces. *SIAM Journal on Scientific Computing*, 39(2):A655–A679, 2017.

[16] John M Girkin and Mariana Torres Carvalho. The light-sheet microscopy revolution. *Journal of Optics*, 20(5):053002, 2018.

[17] Per Christian Hansen. *Discrete inverse problems: insight and algorithms*, volume 7. Siam, 2010.

[18] Per Christian Hansen and Jakob Sauer Jørgensen. Air tools ii: algebraic iterative reconstruction methods, improved implementation. *Numerical Algorithms*, 79(1):107–137, 2018.

[19] Alexander Hertle. The identification problem for the constantly attenuated radon transform. *Mathematische Zeitschrift*, 197(1):13–19, 1988.

[20] Jan Huisken. Slicing embryos gently with laser light sheets. *Bioessays*, 34(5):406–411, 2012.

[21] Jan Huisken and Didier YR Stainier. Even fluorescence excitation by multidirectional selective plane illumination microscopy (mspim). *Optics letters*, 32(17):2608–2610, 2007.

[22] Philipp J Keller and Ernst HK Stelzer. Quantitative in vivo imaging of entire embryos with digital scanned laser light sheet fluorescence microscopy. *Current opinion in neurobiology*, 18(6):624–632, 2008.

[23] Joseph R Lakowicz. *Principles of fluorescence spectroscopy.* Springer Science & Business Media, 2013.

[24] S Lam, F Lesage, and X Intes. Time domain fluorescent diffuse optical tomography: analytical expressions. *Optics Express*, 13(7):2263–2275, 2005.

[25] Jizhou Li, Florian Luisier, and Thierry Blu. Pure-let image deconvolution. *IEEE Transactions on Image Processing*, 27(1):92–105, 2017.

[26] Fang Hua Lin. A uniqueness theorem for parabolic equations. *Communications on Pure and Applied Mathematics*, 43(1):127–136, 1990.

[27] James G Nagy and Zdenek Strakos. Enforcing nonnegativity in image reconstruction algorithms. In *Mathematical Modeling, Estimation, and Imaging*, volume 4121, pages 182–190. International Society for Optics and Photonics, 2000.

[28] Vasilis Ntziachristos. Fluorescence molecular imaging. *Annu. Rev. Biomed. Eng.*, 8:1–33, 2006.

[29] Omar E Olarte, Jordi Andilla, Emilio J Gualda, and Pablo Loza-Alvarez. Light-sheet microscopy: a tutorial. *Advances in Optics and Photonics*, 10(1):111–179, 2018.

[30] Emmanuel G Reynaud, Uroš Kržič, Klaus Greger, and Ernst HK Stelzer. Light sheet-based fluorescence microscopy: more dimensions, more photons, and less photodamage. *HFSP journal*, 2(5):266–275, 2008.

[31] Emmanuel G Reynaud, Jan Peychl, Jan Huisken, and Pavel Tomancak. Guide to light-sheet microscopy for adventurous biologists. *Nature methods*, 12(1):30, 2014.

[32] Jörg G Ritter, Jan-Hendrik Spille, Tim Kaminski, and Ulrich Kubitscheck. A cylindrical zoom lens unit for adjustable optical sectioning in light sheet microscopy. *Biomedical optics express*, 2(1):185–193, 2011.

[33] Bruno Rossi and Kenneth Greisen. Cosmic-ray theory. *Reviews of Modern Physics*, 13(4):240, 1941.

[34] Leonid I Rudin, Stanley Osher, and Emad Fatemi. Nonlinear total variation based noise removal algorithms. *Physica D: nonlinear phenomena*, 60(1-4):259–268, 1992.

[35] Peter A Santi. Light sheet fluorescence microscopy: a review. *Journal of Histochemistry & Cytochemistry*, 59(2):129–138, 2011.

[36] Donald C Solmon. The identification problem for the exponential radon transform. *Mathematical methods in the applied sciences*, 18(9):687–695, 1995.

[37] Plamen Stefanov. The identification problem for the attenuated x-ray transform. *American Journal of Mathematics*, 136(5):1215–1247, 2014.

[38] Florian Stuker, Jorge Ripoll, and Markus Rudin. Fluorescence molecular tomography: principles and potential for pharmaceutical research. *Pharmaceutics*, 3(2):229–274, 2011.

[39] Zhou Wang, Alan C Bovik, Hamid R Sheikh, Eero P Simoncelli, et al. Image quality assessment: from error visibility to structural similarity. *IEEE transactions on image processing*, 13(4):600–612, 2004.